A Thesis Presented to

The Faculty of Alfred University

Synthesis and characterization of reduced niobates for thermoelectric applications

Samuel A. Miller

In Partial Fulfillment of
the Requirements for
The Alfred University Honors Program

Date May 9, 2013

Under the Supervision of:

Chair: Dr. Scott Misutre (signature)

Committee Members:

Dr. Doreen Edwards (signature)

Dr. Steven Pilgrim (signature)

Table of Contents

Title Page……..i

Table of Contents…….ii

List of Tables…….....iii

List of Figures……iv

Abstract……v

1. INTRODUCTION……1

A. Thermoelectric Materials……1

B. Thermoelectric Property Considerations……2

C. Electronic Considerations……...3

D. Reduced Niobates as Thermoelectric Candidates……...4

2. EXPERIMENTAL PROCEDURES…….....5

A. Synthesis…….5

B. Phase and Microstructural Characterization……...6

C. Thermoelectric Characterization……7

3. RESULTS AND DISCUSSION……9

A. Overview…….9

B. High Temperature X-ray Diffraction and Phase Purity……10

C. Microstructural Characterization…….....……...13

D. Reproducibility and Stability of Reduced Niobates…….……15

E. Electrical Conductivity as a Function of Sintering Parameters…….……17

F. Electrical Conductivity as Function of Dopant Levels…….……17

G. Thermal Conductivity Results……..……19

4. CONCLUSIONS……..……20

5. FUTURE WORK…….21

6. ACKNOWLEDGEMENTS……21

7. REFERENCES….……22

LIST OF TABLES

Table I. Various sintering parameters to achieve desired phase. ……7
Table II. EDS results for 2% Cr 6h 1450°C sample. ……13
Table III. EDS results for 4% Cr 3h 1450°C sample. ……..……14

LIST OF FIGURES

Figure 1. Demonstration of design of thermoelectric device……..……..2
Figure 2. Displacement of Nb within NbO_6 octahedra……...…….5
Figure 3. Setup of housing for conductivity and Seebeck coefficient testing…….……9
Figure 4. Overview of steps taken during research project …….….10
Figure 5. *In-situ* high temperature X-ray diffraction of Nb_2O_5……...……..11
Figure 6. *In-situ* XRD measurement showing temperature where phases appear…….…12
Figure 7. X-ray diffraction pattern of surface and bulk of sample……12
Figure 8. 1kx BSE image of 2% Cr 6h 1450°C sample…….13
Figure 9. 1kx BSE image of 4% Cr 3h 1450°C sample…….14
Figure 10. X-ray diffraction pattern of as-sintered and annealed samples……15
Figure 11. Conductivity and Seebeck coefficient for as-sintered and annealed…….…...16
Figure 12. Electrical conductivity and Seebeck coefficient for two separate trials……...16
Figure 13. The effect of microstructure due to sintering time on conductivity…….17
Figure 14. The effect of dopant conc. on conductivity and Seebeck coefficient…….…..18
Figure 15. The activation energy of 4% Cr 1450°C 3h…….……19
Figure 16. Thermal conductivity and heat capacity data for varying dopant levels……..20

Abstract

Niobia was reduced in 4% H_2-96% N_2 to form various Magneli shear structured phases with composition $NbO_{2.5-\gamma}$. Phases were confirmed using powder X-ray diffraction and imaged using SEM which, combined with EDS, revealed phase separation in the compacts. Dopants of Fe_2O_3 and Cr_2O_3 were added in 2 and 4 atomic percent amounts. Properties, such as electrical conductivity, Seebeck coefficient, and thermal conductivity, of various structure types and dopant levels were measured from 250-950°C in an inert atmosphere. The effect of dopant level, sintering time, and annealing on electrical conductivity and Seebeck coefficient were studied. It was found that $Nb_{12}O_{29}$ can be formed over a range of temperatures by sintering in 4% H_2 but that refinement is necessary to produce phase purity. Control of sintering parameters was found to be important in controlling the phase identity and purity formed, the grain size, and surface reduction. Based on electrical conductivity data a hypothesis is put forward; that oxygen vacancies controlled conduction at low temperature and chromium substitutions on niobium sites controlled at higher temperatures, though more study is needed to confirm this. Lastly, phase stability of these structures was demonstrated up to 1000°C in an inert atmosphere demonstrating that these materials are viable for thermoelectric applications.

1. INTRODUCTION

Energy is wasted in nearly all systems and power generation is no different; a huge amount of heat is lost in automotive and industrial heating applications, it is estimated that about 25% of the energy in fuel is used to propel the vehicle whereas 40% of the energy is lost in the form of heat.[i] Therefore efficient, stable thermoelectric materials are needed to capture and utilize this wasted heat.

A. Thermoelectric Materials

The thermoelectric effect has been understood in some form for around 200 years and can be divided into three different effects, the Seebeck, Peltier, and Thomson effects, each of which could be utilized in its own right. But to efficiently run thermoelectric devices to convert temperature gradients to electricity, a high Seebeck coefficient is needed.[ii] Thermoelectric materials are ones that convert a temperature gradient to a voltage and the Seebeck coefficient is a measure of how efficiently this is done by the material. Current materials leading in efficiency are semiconductors that combine intermetallics such as SiGe, PbTe, and Bi_2Te_3, but these oxidize and decompose at high temperatures and none are environmentally friendly, thus much research has been centered on oxide thermoelectric materials due to their stability and environmental friendliness.[iii] Oxide materials are typically poor electronic conductors due to low carrier mobility; however, recent advances have been made in Na_xCoO_2 and a number of other doped oxides, mostly p-type, producing ZT values competitive with those of semiconductors.[iv]

Devices are formed by assembling two dissimilar materials in a series; *p*-type and *n*-type semiconductors are aligned thermally in parallel but electrically in series as seen in Figure 1. Materials that are *p*-type have an excess of holes (a hole means an absence of an electron) whereas ones that are *n*-type have extra electrons. As one side of the device is subjected to heating, electrons from the *n*-type material flow to cold side along with holes from the *p*-type material, thus causing a voltage gradient. The materials in these devices must be paired with materials of similar Seebeck coefficient and thermal expansion to maximize the efficiency and lifetime, respectively, of the device. Thus it is

important to develop new materials, especially stable oxides, which meet these requirements.

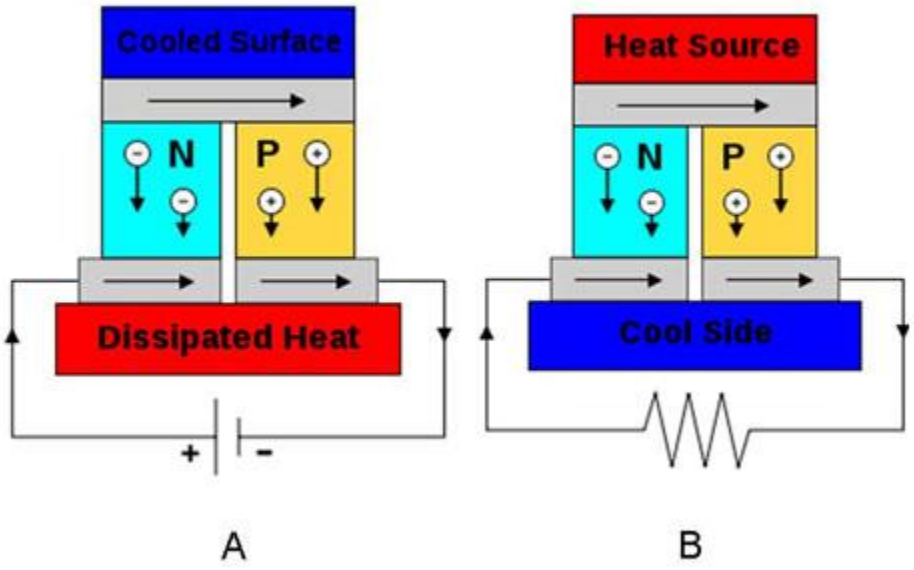

Figure 1. Demonstration of design of thermoelectric device. [v]

B. Thermoelectric Property Considerations

The performance of thermoelectric materials is defined by the dimensionless figure of merit $ZT = T\times(S^2\sigma)/\kappa$, where T is the absolute temperature, S is the Seebeck coefficient, σ is the electrical conductivity, and κ is the thermal conductivity. Ideally, ZT must be ~1.0 or greater to be commercially applicable[vi]. The best performance is attained when the Seebeck coefficient and electrical conductivity are maximized and the thermal conductivity is minimized. This relationship is described as "phonon glass, electron crystal" behavior which means that the electrons should experience the material as a crystal with ease of conductivity but the phonons should experience it as a glass with high scattering. [vii]

The Seebeck coefficient, also known as the thermopower, is described by the equation $\Delta V=S*\Delta T$, thus by plotting change in voltage against the change in temperature, S can be found by determining the slope. For *n*-type materials the Seebeck coefficient is negative while for *p*-type S>0. The electrical conductivity, σ, can happen by a number of

mechanisms which will be discussed following. Thermal conductivity is a combination of both phonon (lattice) and electronic contributions, with most ceramics having a κ of ~1-2 $Wm^{-1}K^{-1}$. To obtain efficient power generation the temperature gradient and ZT must be maximized but since ZT itself is a function of temperature, as are the properties that make it up, materials must be tailored to perform desirably.

C. Electronic Considerations

Oxides can conduct by a number of mechanisms, namely ionic, band, or polaron hopping conduction, but they are typically known for their dielectric properties. Metallic or semiconducting behavior can be achieved by controlling the defect chemistry through dopants; donor and acceptor ions can be added to produce *n*- and *p*- type conductors. Materials that are *p*-type have an excess of holes (a hole means an absence of an electron) whereas ones that are *n*-type have extra electrons. For example, if you take the typical semiconductor, silicon which has four outer shell electrons, and dope it with gallium, which has only 3, this causes the structure to be missing one electron where the gallium has taken the place of the silicon, thus creating a *p*-type material. Conversely, doping Si with phosphorus creates a *n*-type material. In my case, reducing in a hydrogen atmostphere means that the hydrogen gas reacts with some of the oxygen in the niobia, leaving the material with missing oxygen atoms, thus creating a material that is n-type and conducts via an oxygen vacancy mechanism. Conduction type is determined by both the constituent ions as well as the structure and is not always easily determined. Conductivity is given by the equation $\sigma=ne\mu$, where n is the carrier concentration, e is the charge, and μ is the mobility of the carrier. It is important to note that the conductivity is the sum of the all the mechanisms of charge transport. This gives rise to a problem in the thermoelectric efficiency in that conductivity increases with number of charge carriers whereas Seebeck coefficient, a measure of the entropy per carrier, decreases with increasing carrier concentration. [viii]

Band theory describes the conduction mechanism of broad band conductors; charge carriers must exceed the band gap, essentially the activation energy, before they can conduct. This energy comes in the form of thermal energy so that at higher temperatures more carriers are able to overcome the band gap but mobility is decreased

as increased lattice vibrations decrease the mean free path. If the conduction mechanism is by band conduction then a plot of $ln(\sigma)$ vs. $1/T$ will indicate the activation energy, E_a, which is equal to the slope times Boltzmann's constant. This is only true though for intrinsic semiconductors whereas in semiconducting oxides, oxygen vacancies can act as donors and reduce the activation energy to a value smaller than that of the band gap.

Polarons are created when charged species, moving through the through an ionic lattice, become localized on an ionic species. This causes electronic conduction to be more similar to diffusion than to broad band conduction as the polaron can only hop to unoccupied sites. The energy barrier for this mechanism of the charged species jumping from one site to and adjacent, unoccupied, site can also be overcome through thermal energy but it exhibits a diffusion-like temperature dependence. For this mechanism straight line slope indicates the activation energy, a combination of the contributions to both carrier generation and mobility, over k_B when plotted on a graph of $ln(\sigma T)$ vs. $1/T$.

D. Reduced Niobates as Thermoelectric Candidates

Thermoelectric devices must have two sides, p-type and n-type, but progress in n-type oxides has lagged far behind that of p-type. Some of the highest ZT values in n-type materials have been reported in doped strontium titanates[ii] and nanostructured ZnO.[ix] Ferroelectric behavior has previously been linked to high thermoelectric power, $S^2\sigma$, in oxide materials such as $BaTiO_{3-\delta}$ and $(Sr_{1-x}Ba_x)Nb_2O_{6-\delta}$, though the mechanisms remain unclear.[i]

Few authors have studied or reported on the thermopower of reduced niobates, Cheng, et al.[x] being one of them, but much work has been done characterizing the family of reduced Nb_2O_5, specifically $Nb_{12}O_{29}$. It can form into either a monoclinic or orthorhombic crystallographic shear plane structure that exhibits metallic conductivity above 4 K,[xi, xii] which forms due to the inability of Nb_2O_5 to tolerate oxygen deficiencies. Therefore particular care must be taken to produce single phase samples. This is usually accomplished using a niobium metal gettering technique in a vacuum but this research suggests it could be accomplished by a reducing atmosphere if properly controlled.

The conductivity of these structures is shown to relate to their oxygen vacancies[xiii] and is metallic like over a wide range of temperatures.[xiv] The defect reaction for the reduction and doping of Nb_2O_5 is as follows:

$$Cr_2O_3 + 6\ Nb_2O_5 + 2\ H_i^{\bullet} \rightarrow 2\ Cr_{Nb}^{''} + Nb_{12}O_{29} + 3\ V_O^{\bullet\bullet} + H_2O$$

It should be noted that the reduction to $Nb_{12}O_{29}$ leads to the production of two Nb^{4+} ions from Nb^{5+} ions as well as two of the three oxygen vacancies whereas the doping with Cr^{3+} on Nb^{5+} sites only results in one oxygen vacancy. McQueen, et al.[xiii] found that the structure of NbO_6 octahedra in both the $Nb_{12}O_{29}$ and $Nb_{22}O_{54}$ compounds are very similar with Nb ions being displaced within them, shown in Figure 2, thus the antiferroelectric ordering of the electric dipoles. The electronic properties arise from the presence of Nb^{4+} ions, which are not localized, of which the concentration increases as niobia is reduced from Nb_2O_5 to $Nb_{12}O_{29}$. On the other hand Llunell, et al.[xiv] suggested that there may both localized and delocalized electrons in the Nb1-Nb1 bond, though there is just one type of symmetry, as an explanation to the existence of both antiferromagnetism and metallic conductivity in this structure. Furthermore, Waldron, et al.[vii] has shown $Nb_{12}O_{29}$ to be anti-ferromagnetically ordered; thus these reduced niobates provide a new platform on which to understand thermoelectric properties.

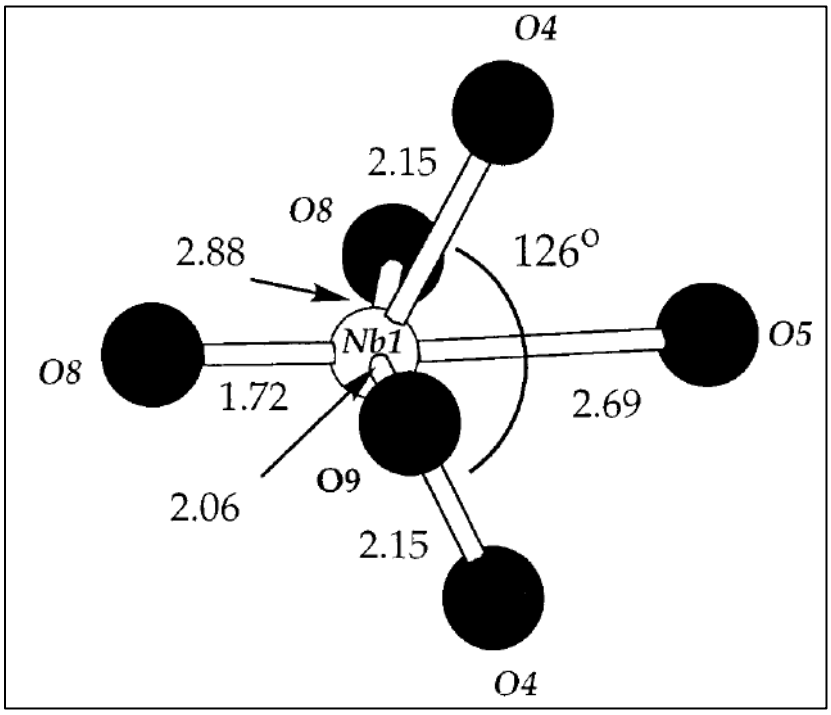

Figure 2. Displacement of Nb within NbO_6 octahedra. [xv]

2. EXPERIMENTAL PROCEDURES

A. Synthesis

Standard laboratory grade Nb_2O_5 was used as the precursor; this was measured into 5 to 7 gram quantities before being pressed into pellets to aid in densification. Oleic acid was applied to the tungsten die and rams as a lubricant using a cotton swab prior to each pelletization. The powder was then added and the rams pressed together to remove excess air before hydraulically pressing. Using a uniaxial press and 1 inch diameter die, loads were applied from 0 to 4000 lbs (~35 MPa) in 5 steps, releasing the pressure between each step. The final press of 4000 lbs was then held for 30 seconds before being released, after which the pellet was removed.

Upon determination of proper reduction parameters, a number of dopants were added on an atom percentage basis. After calculating the desired amount of each material, the oxides were once again weighed out to a total of 7 grams. Dopants used include Fe_2O_3 and Cr_2O_3, though iron oxide was not compatible in producing pellets of uniform cross section and was thus not investigated further. Batches were then added to a cylindrical vibratory mill with cylindrical alumina media along with isopropanol and shaken for 10 minutes. Compositions included $Cr_xNb_{2-x}O_5$ and $Fe_xNb_{2-x}O_5$, where x = 0.02 and 0.04; samples of the same dopant were made on the same day, thus the container and milling media were cleaned between each use with sand and DI water with the lower dopant content always being mixed first. Upon completion of the milling, the powder and isopropanol mixture was poured through a strainer and the container and media were rinsed with more isopropanol. This was all collected in a drying pan which was then placed on hot plate turned to medium-low in a fume hood. When the isopropanol had evaporated leaving a uniformly mixed powder, this was then subjected to the same pelletizing technique as described previously.

B. Phase and Microstructural Characterization

In order to synthesize the desired $Nb_{12}O_{29}$ phase various temperature, time, and atmosphere parameters were attempted which are summarized in Table I.

Table I. Various sintering parameters to achieve desired phase.

Dopant	Temperature (°C)	Hold time (h)	Atmosphere (remainder is N_2)	Resulting phase
N/A	1300	6	4% H_2	Nb_2O_5
N/A	1300	3	100% H_2	NbO_2
N/A	1300	3	50% H_2	NbO_2
N/A	1450	6	4% H_2	$Nb_{22}O_{54}$
2% Cr	1450	6	4% H_2	$Nb_{22}O_{54}$+ NbO_2
4% Cr	1450	6	4% H_2	$Nb_{12}O_{29}$
2% Fe	1450	6	4% H_2	$Nb_{12}O_{29}$
4% Fe	1450	6	4% H_2	$Nb_{12}O_{29}$
2% Cr	1450	3	4% H_2	$Nb_{22}O_{54}$+ NbO_2
4% Cr	1450	3	4% H_2	$Nb_{22}O_{54}$+NbO_2
2% Fe	1450	3	4% H_2	$Nb_{12}O_{29}$+NbO_2
4% Fe	1450	3	4% H_2	$FeNb_{11}O_{29}$+NbO_2
N/A	1365	24	4% H_2	$Nb_{12}O_{29}$+NbO_2

2% Cr	1365	24	4% H_2	$Nb_{22}O_{54}$+NbO_2
4% Cr	1365	24	4% H_2	$Nb_{22}O_{54}$+NbO_2

After reduction of pellets was finished, pellets were analyzed using XRD to determine what phase(s) formed. A Bruker D8 Advance powder X-ray diffractometer was used with copper Kα radiation at 45 kV and 40 mA. Scans were performed from 3-70° 2θ as a Coupled Theta/Two Theta and Continuous PSD fast scan on either a flat pellet surface or finely ground powder sample with 0.2 seconds taken at each step. High temperature *in-situ* X-ray diffraction was performed using a customized furnace in a standard Siemens D5000 X-ray diffractometer. To conduct phase analysis, Jade 9 (Materials Data Inc., U.S.A.) was used. A representative group of samples was selected to undergo an annealing process after reduction consisting of a ramp of 5°C/min and a hold of 24 hours at 1000°C in a nitrogen atmosphere to confirm phase stability.

The microstructure of unetched fracture surfaces of samples was characterized using a FEI Co., Inc. Quanta 200F field emission scanning electron microscope equipped with an EDAX Genesis energy-dispersive spectrometer.

C. Thermoelectric Characterization

Bars were cut from the pellets using a diamond bladed saw on a standard slow speed rotating saw to the approximate dimensions of 3x3x20 mm. Care was taken to produce as uniform cross section as possible though this was not always possible due to warping of the pellets during sintering. The curved ends of the bars were then ground flat using 220 grit sandpaper and notches were filed into the corners, as shown in Figure 3, to create three sections of approximately equal length. Gold paste was subsequently painted on both ends of the bar as well as across the notches to provide electrical contacts; gold wires were wrapped around the bar and sat in the previously made notches.

After preparing the bar for the experiment, it was then loaded into the housing for the thermopower furnace and the gold wires from the bar were attached to leads for thermocouples 2 and 3. This setup is shown in Figure 3. After attaching the wires, the

housing was inserted into the tube furnace and sealed. The furnace was then evacuated using a mechanical pump and backfilled with standard grade Argon gas three times, the last time the gas was allowed to continue flowing at approximately 120 sccm for the duration of the experiment. The pO_2 of the outlet gas was monitored and the furnace was not started until it dropped below 250 ppm. A "bake-out" of 1 hour at 100°C was used at the start of each experiment, after which a ramp rate of 5°C/minute was used followed by a 5 minute dwell once temperature was reached; following the dwell was a 15 minute period holding at the same temperature with measurements taken every 3 minutes for a total of 5 measurements at each temperature interval. Measurements were repeated every 50°C from 100 to 950°C, after which the temperature was decreased in 100 degree intervals to 250°C at the same cooling as ramp rate, with measurements being taken at the end of each drop.

Thermal conductivity was measured using an Anter Flashline 4010 instrument with alumina furnace under flowing high purity argon from 100-600°C. A Clark-Taylor approximation was used correct for the loss of thermal rise due to radiative losses on the irradiated side. Thermal conductivity was then calculated by multiplying the thermal diffusivity by the heat capacity, calculated by reference to a Molybdenum standard, and density.

A MATLAB program was used to analyze the data gathered in these experiments. The contact points are labeled 1, 2, 3, and 4 from the direct connection to the thermocouple on the shown on the left to the connection to the piece of platinum foil on the right of Figure 3, with connections 2 and 3 being made by a gold wire between the bar and thermocouple leads. This means that for each measurement there are 6 data points (1-2, 1-3, 1-4, 2-3, 2-4, 3-4) and 5 measurements at each temperature for a total of 30 data points. The conductivity is just an average of the measurements across each of the contact points but the Seebeck coefficient is calculated by placing data points on a dV/dT plot and using a linear regression to calculate the slope of the best fit line.

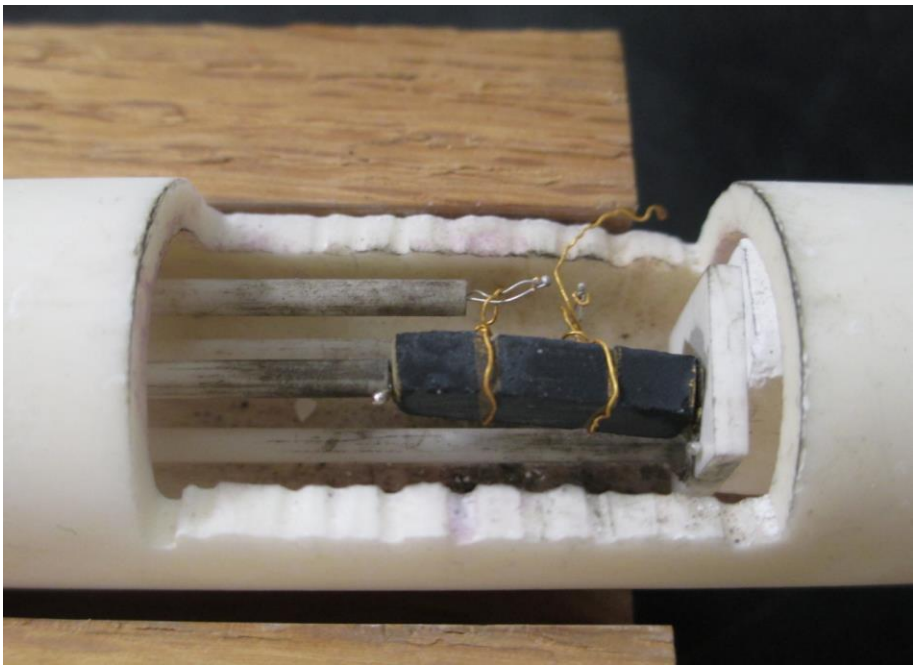

Figure 3. Setup of housing for conductivity and Seebeck coefficient testing. It should be noted that during actual tests the thermocouple beads were wound with the gold wire so that they touched the surface of the bar at the notch. They are away from the surface to show location in this image.

3. RESULTS AND DISCUSSION

A. Overview

Figure 4 serves to outline the steps taken so that the reader has a general idea of the process, results, and direction to complete this research project.

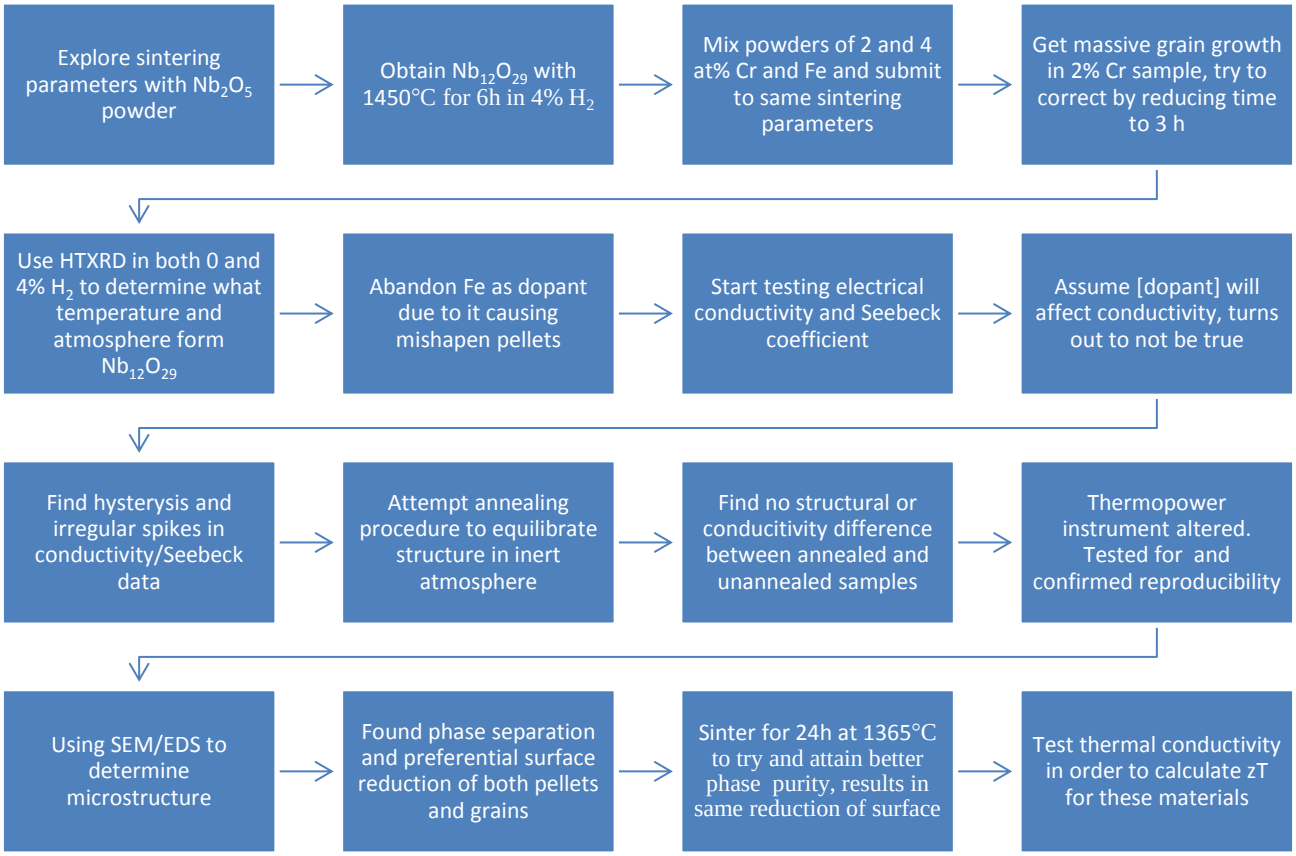

Figure 4. Overview of steps taken during research project serving to outline the process.

B. High Temperature X-ray Diffraction and Phase Purity

High temperature X-ray diffraction shows that upon reduction, a number of phases form at various temperatures in 4% hydrogen. As can be seen in Figure 5, an intermediate phase, $NbO_{2.46}$ which is similar to $Nb_{22}O_{54}$, forms at lower temperatures. In the temperature range of 1350-1375°C $Nb_{12}O_{29}$ forms but upon further heating it is reduced to NbO_2. This demonstrates that it is possible to form phase pure $Nb_{12}O_{29}$ with a hydrogen reduction process, though the difficulty in producing phase pure bulk pellets is still an issue. Figure 6 also shows the stick patterns associated with the temperature at which each of the phases first appeared in the HTXRD experiment.

Another observation that appears significant is the difference between the surface and bulk of nearly all of the prepared samples. X-ray diffraction pattern shows that when

the surface of a pellet is measured, it is often a different phase than the pattern when a piece of the pellet is ground to powder before being measured. This observation is demonstrated in Figure 7.

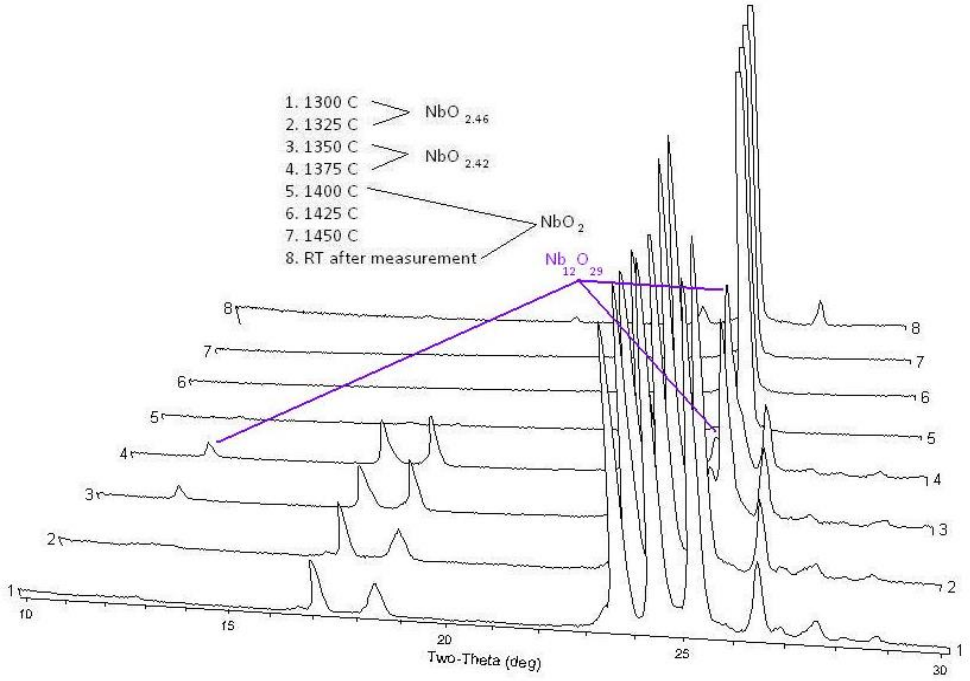

Figure 5. *In-situ* high temperature X-ray diffraction of Nb_2O_5 as it undergoes phase transformation to NbO_2. Unlabeled peaks at temperatures below 1350°C are $NbO_{2.46}$ and above 1375°C are NbO_2. Labeled peaks at 1350-1375°C indicate those used to identify $NbO_{2.42}$ ($Nb_{12}O_{29}$).

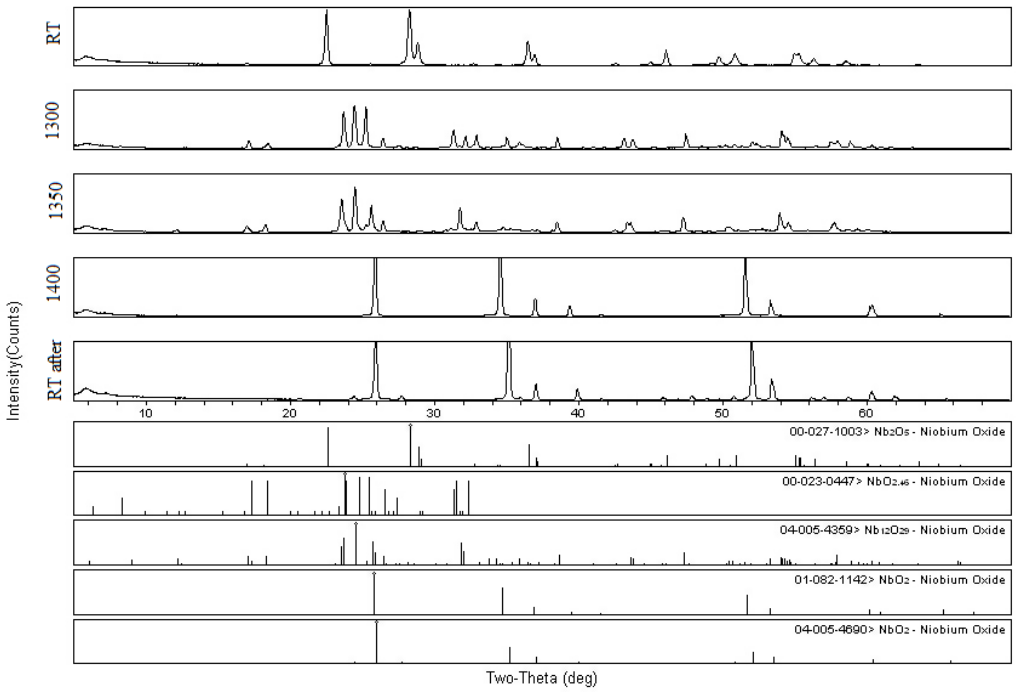

Figure 6. XRD data for *in-situ* measurement showing the temperature at which each phase first appeared. PDF entries are shown below for phase identification.

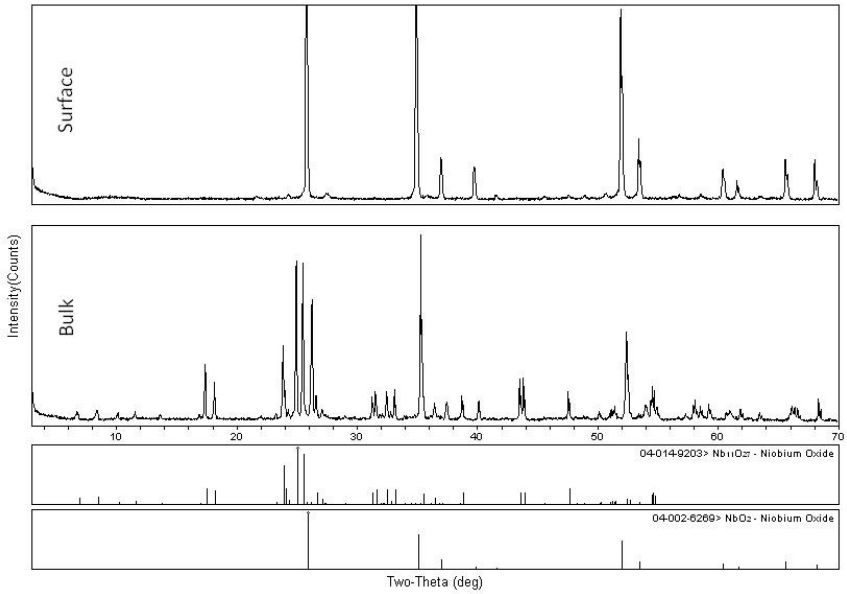

Figure 7. X-ray diffraction pattern of surface and bulk of sample after being cooled from 1365°C following a heat treatment for 24 hours of 4% Cr. PDF entries are shown below for phase identification.

C. Microstructural Characterization

Upon reduction of $Cr_xNb_{2-x}O_5$ where x = 0.02 for 6 hours at 1450°C, the pellet showed exaggerated grain growth on both the top and bottom surface. Further scanning electron microscopy analysis revealed that the material had evolved a discrete secondary phase in a matrix. As can be seen in Table II, EDS revealed that the majority of the chromium resides in the secondary phase and that it is also poor in oxygen compared to the matrix. This result, coupled with X-ray diffraction, suggests that the matrix is $Nb_{22}O_{54}$ while the Cr rich rods (see Figure 8) are NbO_2.

Table II. EDS results for 2% Cr 6h 1450°C sample.

	Matrix		Secondary Phase	
Element	Wt %	At %	Wt %	At %
O	7.1	30.8	4.3	20.6
Nb	92.7	68.9	95.2	78.6
Cr	0.1	0.1	0.5	0.7

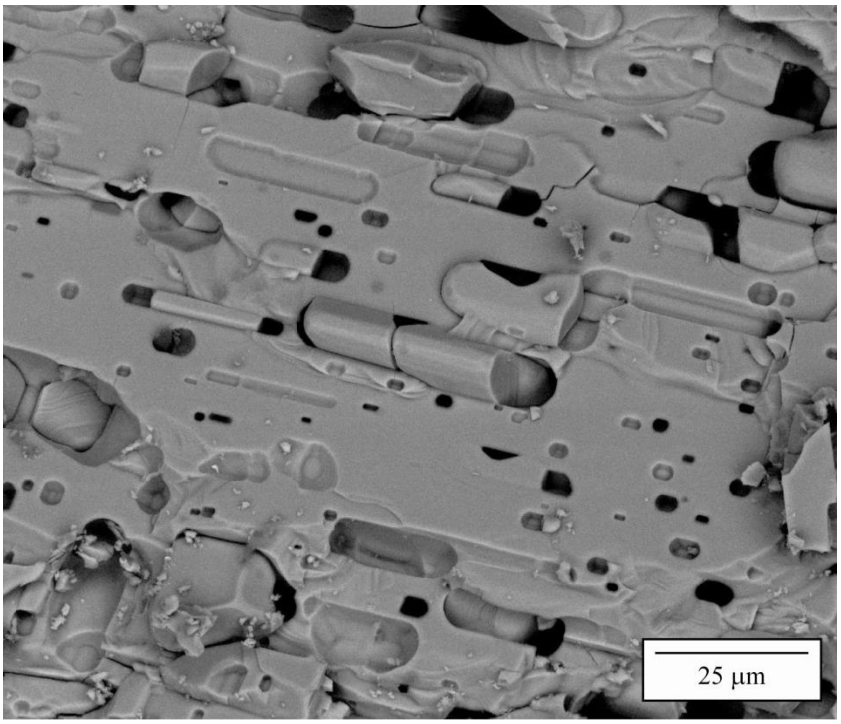

Figure 8. 1kx BSE image of 2% Cr 6h 1450°C sample.

SEM revealed that the 2% Cr 6h 1450°C sample was an exception to the typical microstructure, that the norm is similar to what is observed in the 4% Cr 3h 1450°C sample as seen in Figure 9. In this case it appears that the grains are relatively more oxygenated and that the lamellar phase present on the surface of these grains is poor in both oxygen and chromium as revealed by the EDS results summarized in Table III. This suggests that upon reduction, grains of the desired phase are forming but due to higher mobility or reactivity, the surface and boundaries of these grains are being preferentially reduced. Again this is confirmed by X-ray diffraction that the two phases present are $Nb_{22}O_{54}$ and NbO_2.

Table III. EDS results for 4% Cr 3h 1450°C sample.

	Matrix		Secondary Phase	
Element	Wt %	At %	Wt %	At %
O	7.6	32.4	6.5	28.7
Nb	91.8	66.8	93.2	70.8
Cr	0.4	0.6	0.2	0.3

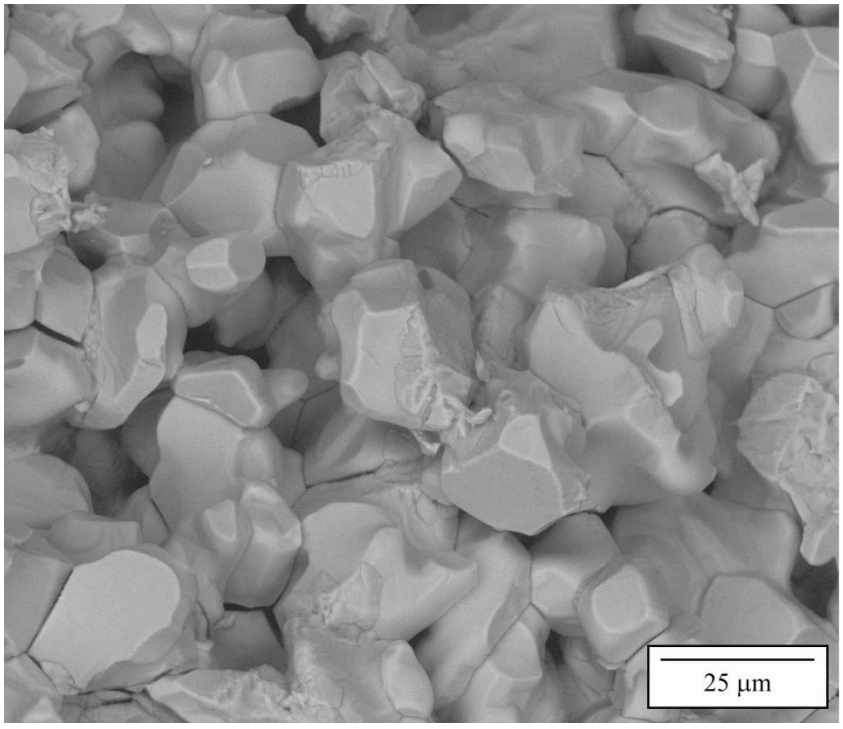

Figure 9. 1kx BSE image of 4% Cr 3h 1450°C sample.

D. Reproducibility and Stability of Reduced Niobates

In order for thermoelectric materials to be viable in a device, they must be stable to reasonably high temperature in non-reducing atmospheres. To prove that these reduced niobates fit this description, samples were annealed in N_2 for 24 hours at 1000°C and X-ray diffraction patterns were compared from before and after this annealing. As can be seen in Figure 10, there is not a significant difference between the sample before and after the annealing process nor after a thermopower measurement.

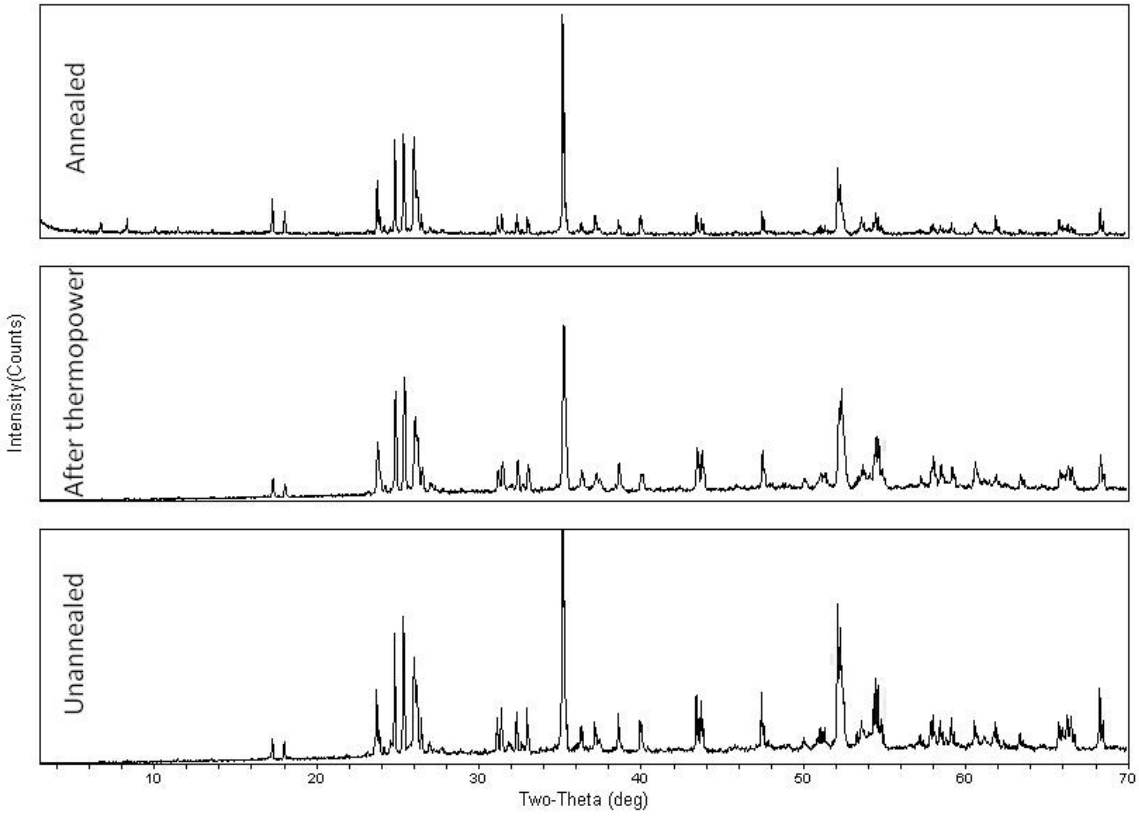

Figure 10. X-ray diffraction patterns of as-sintered and annealed samples for 4% Cr 3h.

Additionally, the conductivity and Seebeck coefficient were measured for the same bar of the same sample, 4% Cr reduced at 1450°C for 3 hours, both before and after the annealing process. Again, Figure 11 shows that there is not a significant difference in either the conductivity or Seebeck coefficient between the two measurements. Furthermore it is shown in Figure 12 that the results of these tests are reliable and reproducible. Although the Seebeck coefficient does vary somewhat, staying within +/- 20 μV/K, the conductivity of the two trials matches very well.

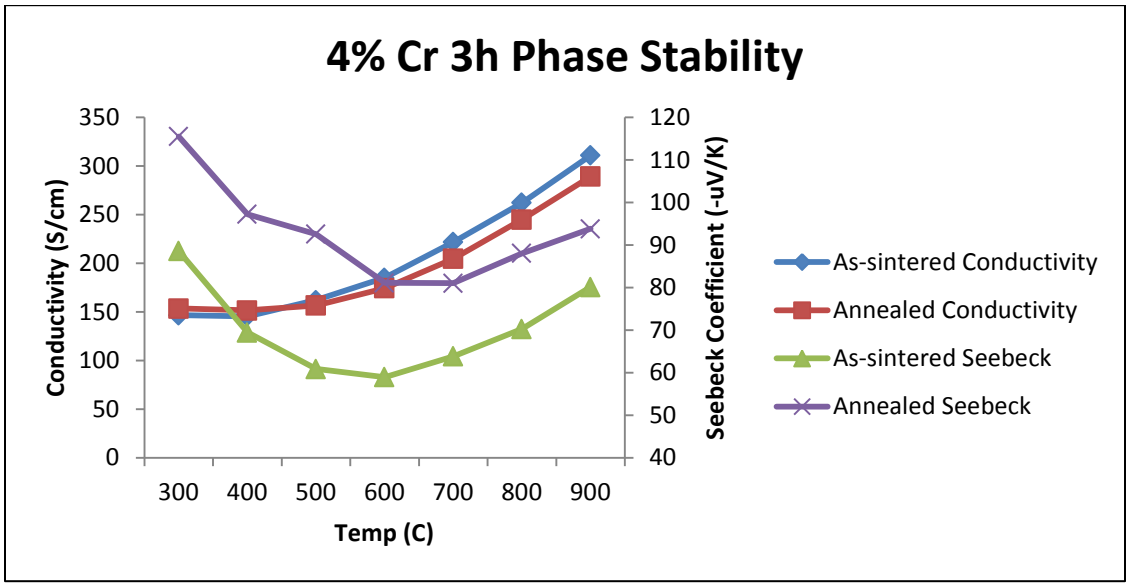

Figure 11. Electrical conductivity and Seebeck coefficient for 4% Cr 3h 1450°C sample both before and after annealing process.

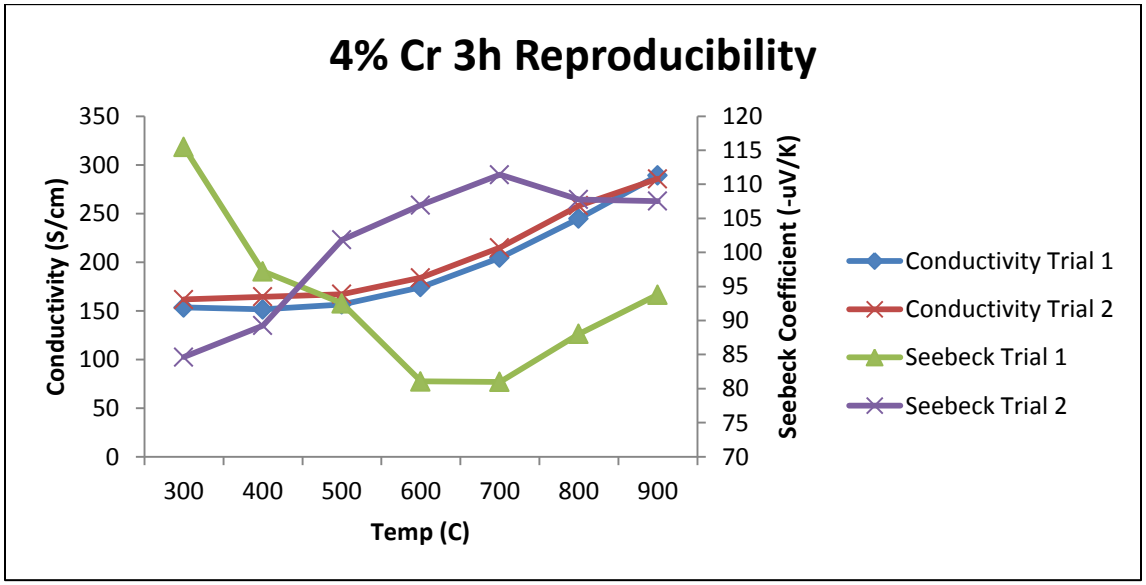

Figure 12. Electrical conductivity and Seebeck coefficient for 4% Cr 3h 1450°C sample for two separate trials.

E. Electrical Conductivity as a Function of Sintering Parameters

By comparing the electrical conductivity of two samples with the same composition but differing length of sintering time, it was determined that grain growth behavior due to sintering parameters affected conductivity. This can be seen in Figure 13 which shows that the conductivity of the 2% Cr sample that was reduced for only 3 hours is four times larger than that of the sample reduced for 6 hours. The same effect is seen in the 4% Cr sample but not to the same magnitude. The abnormally large grains in the $Cr_xNb_{2-x}O_5$ where x = 0.02 sample that was sintered for 6 hours is likely part of the reason for its much lower conductivity. These large grains were not observed in the $Cr_xNb_{2-x}O_5$ where x = 0.04 sample that was also sintered for 6 hours thus indicating that microstructure due to sintering time plays a role in the behavior of these materials.

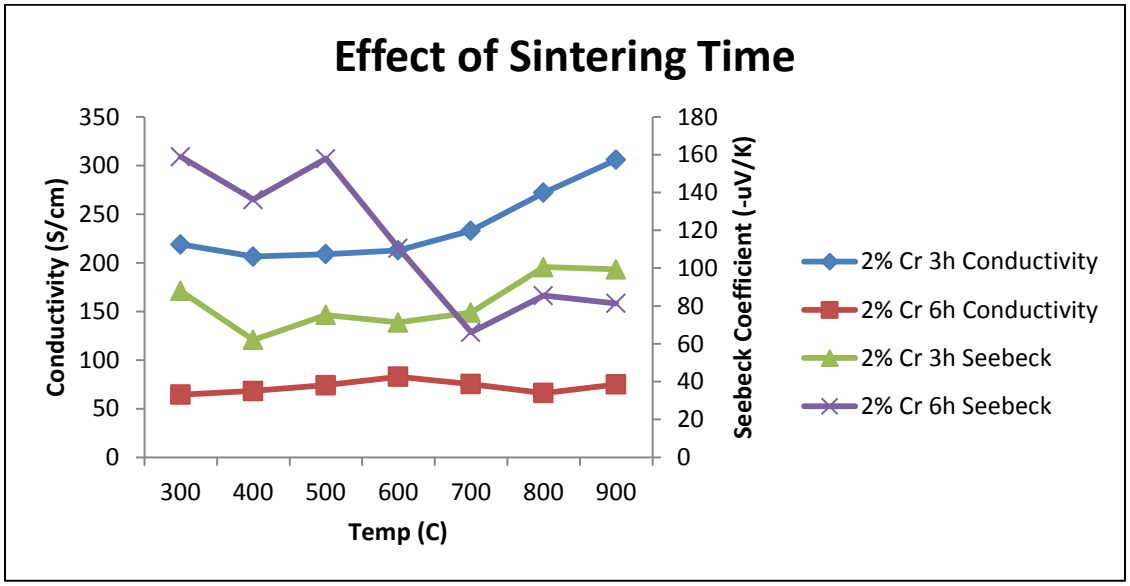

Figure 13. The effect of microstructure due to sintering time is shown by comparing samples of the same composition but different sintering parameters.

F. Electrical Conductivity as a Function of Dopant Levels

It was assumed that conductivity would increase with increased dopant concentration due to a higher carrier concentration. As shown in Figure 14 this is not necessarily true. The 2% Cr sample has a higher conductivity initially but as temperature increases, the rate at which the conductivity increases is not as great as that of 4% Cr so

at high temperatures their conductivity is the same. Conversely, the Seebeck coefficient is the same for the two samples at low temperature but deviates at higher temperatures. A proposed explanation for the effect seen here is that there are two temperature regimes in which different conduction mechanisms dominate; at low temperature the dominant charge carrier is oxygen vacancies but at high temperature it is the Cr for Nb substitution. If there was an interaction between the dopant and the oxygen vacancies then it is possible that the distortion of the structure due to chromium dopants could lower the conductivity in the $Cr_{0.04}Nb_{1.96}O_5$ sample. Likewise, at higher temperature as the electrical conductivity of the 4% Cr sample increases at a faster rate than that of the 2% Cr sample, the thermal conductivity would also be rising faster, thus leading to the lower Seebeck coefficient observed. It should be noted that this is simply a possible explanation to the observed trends as there is not enough information to state the mechanisms with certainty.

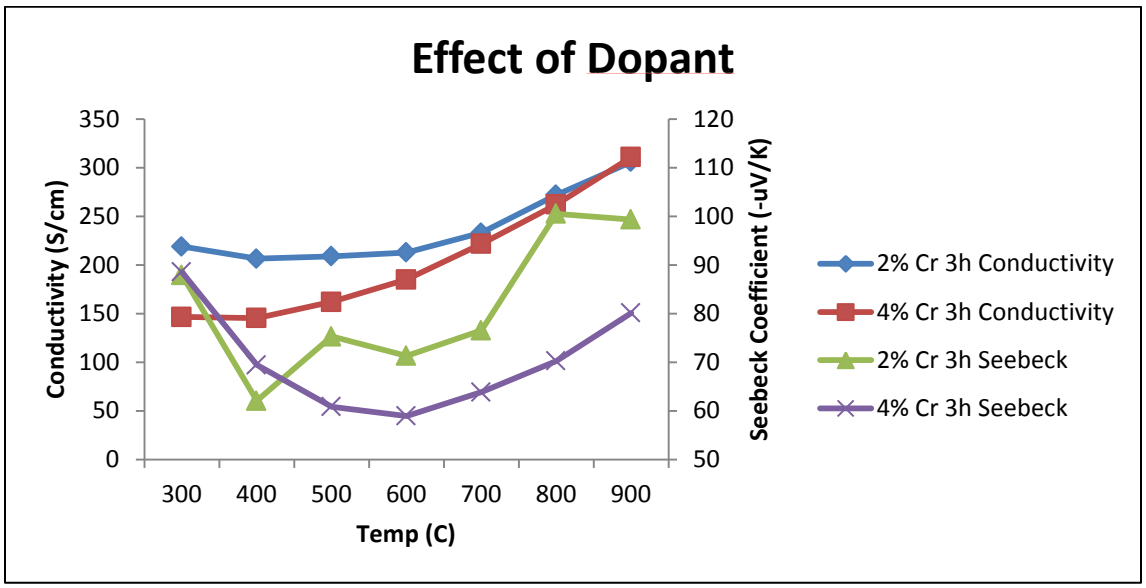

Figure 14. The effect of dopant concentration on the electrical conductivity and Seebeck coefficient is shown.

From a plot of ln(σ) against 1/T in Kelvin it is possible to determine the activation energy for conduction by multiplying the slope of the line by Boltzmann's constant. For these materials, there appears to be two distinct regions with differing activation energies;

in the high temperature region on the left side of Figure 15 the activation energy is 0.105 eV and for the low temperature region E_a = 0.034 eV. Typically activation energies of this magnitude indicate either band conduction or small polaron conduction so this information, combined with the temperature dependence observed in all samples indicates that the mechanism is most likely band conduction. The explanations for the existence of two activation energies in two temperature regions are numerous, such as orientation in *k* space or a subtle structure change at high temperature but no conclusions can be drawn from this data without additional defect chemistry studies.

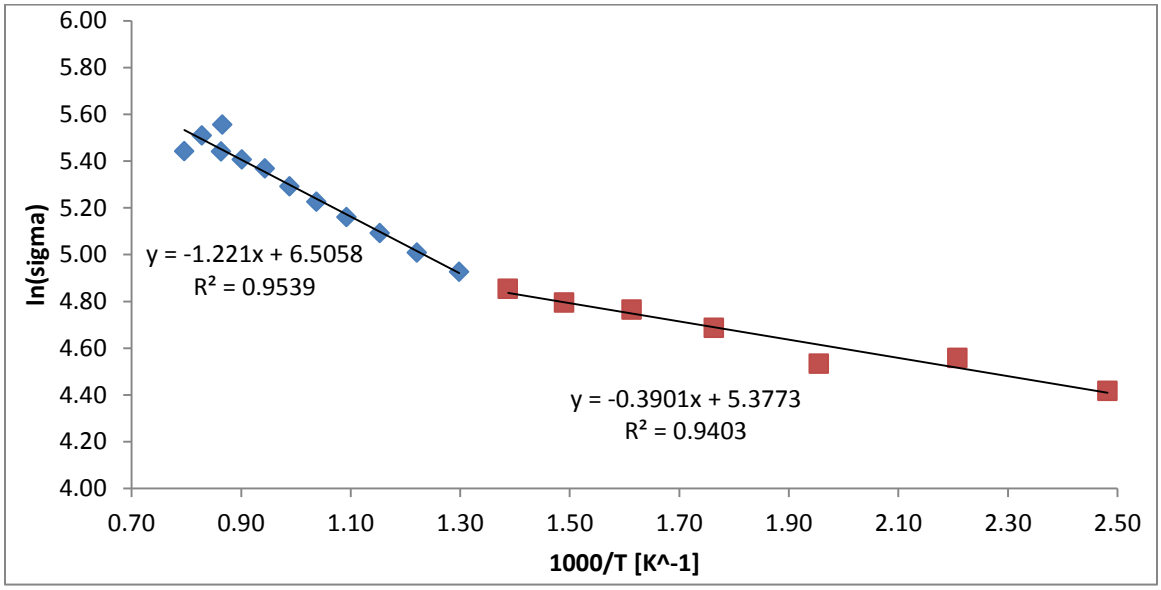

Figure 15. The activation energy of 4% Cr 1450°C 3h.

G. Thermal Conductivity Results

It can be seen in Figure 16 that the general trend is an increasing thermal conductivity as dopant level increases. Due to the increased carrier concentration as the concentration of dopant is increased, this makes intuitive sense but it should be noted that the pellets used to carry out this measurement were not of uniform density so it is unwise to cite absolute conductivity values, though the trends should hold true.

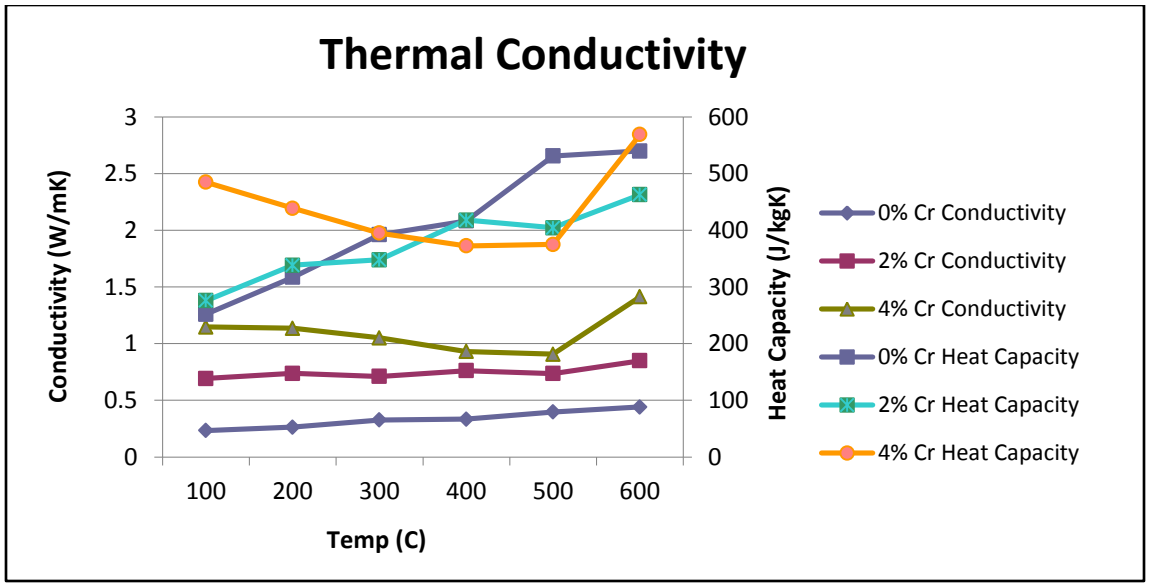

Figure 16. Thermal conductivity and heat capacity data for varying dopant levels.

4. CONCLUSIONS

It was found that reduced niobates, specifically the more reduced phases of $Nb_{12}O_{29}$ and $Nb_{22}O_{54}$, are good candidates for thermoelectric applications; they show high conductivities in excess of 300 S/cm at high temperatures, reasonably large Seebeck coefficients on the order of -100 μV/K, and small thermal conductivities. Assuming a thermal conductivity of 1 W/mK, the highest ZT value for the reduced niobates studied was 0.39 in the sample that was doped with 4%, sintered in 4% H_2 for 3 hours, and annealed in N_2. This high ZT value makes these materials worthy of additional work as *n*-type oxide thermoelectric.

Niobia was reduced to form various Magneli shear structured phases with composition $NbO_{2.5-\gamma}$, with the ultimate goal of producing $Nb_{12}O_{29}$. It was found the $Nb_{12}O_{29}$ structure can be formed over a range of temperatures and sintering times in 4% H_2 but that more refinement is needed to produce phase pure samples. The findings that both the surface of most pellets as well as the grains within those pellets are further reduced than the bulk indicates that the mechanism of hydrogen diffusion occurs via a grain boundary mechanism. It was also found that grain size due to sintering time greatly affected conductivity which also suggests that the conduction mechanism is one that is dependent on the grain boundary mechanism. As noted before, the electrical conduction

in this system is very complicated, having two different mechanisms in different temperature regimes. A hypothesis was put forward based on observed data, that oxygen vacancies controlled conduction at low temperature and chromium substitutions on niobium sites controlled at higher temperatures, though more study is needed to confirm this. It is important to note that both reduction and doping contribute to both conductivity and Seebeck coefficient in their creation of oxygen vacancies, Nb^{4+} ions, and Cr_{Nb} substitutions, though more study is needed to determine the exact contributions. Lastly, phase stability of these structures was demonstrated up to 1000°C in an inert atmosphere demonstrating that these materials are viable for thermoelectric applications.

5. FUTURE WORK

Further investigation of a few points is necessary to understand the phenomena occurring in this reduced niobate system. As the diffusion of hydrogen is assumed to be fast, it would be interesting determine the diffusion behavior in this structure as both the surface of the pellet as a whole as well as the surface of individual grains is more reduced than the bulk. The results of this study might indicate the sintering parameters that would lead to optimization of both phase purity and densification behavior. Additional work is also needed to confirm the defect chemistry and conduction mechanisms in the two temperature regimes.

6. ACKNOWLEDGEMENTS

I would like to thank Dr. Misture for his guidance on this project, Peter Metz for his assistance and recommendations, and Drs. Edwards and Pilgrim for being on my Honors Committee.

7. REFERENCES

[i] F. Stabler, "Automotive applications of high efficiency thermoelectric" (2002) *DARPA/ONR/DOE high efficiency thermoelectric workshop*; pp. 1–26.

[ii] S. Lee, et al., "Ferroelectric-thermoelectricity and Mott transition of ferroelectric oxides with high electronic conductivity," *J Eur Ceram Soc,* **32** (2012).

[iii] J.W. Park, et al., "Thermoelectric properties of Bi, Nb co-substituted $CaMnO_3$ at high temperature," *J. Alloys Compd.,* **47** (2009).

[iv] I. Terasaki, Y. Sasago, and K. Uchinokura, "Large thermoelectric power in $NaCo_2O_4$ single crystals," *Phys. Rev. B,* **56** (1997).

[v] D.B. Whyte, "Icy Hot Electricity: The Thermoelectric Effect" (2013) Science Buddies. Accessed on: Januuary 2013. Available at < http://www.sciencebuddies.org/science-fair-projects/project_ideas/Elec_p055.shtml >

[vi] H. Ohta, K. Sugiura, and K. Koumoto, "Recent progress in oxide thermoelectric materials: p-type $Ca_3Co_4O_9$ and n-type $SrTiO_3$," *Inorg. Chem.,* **47** (2008).

[vii] G.A. Slack, D.M. Rowe (Ed.), *CRC Handbook of Thermoelectronics*; pp. 407–440. CRC Press, Boca Raton, FL, 1995.

[viii] Y. Pei, X. Shi, A. L. H. Wang, L. Chen, and G. J. Snyder, "Convergence of electronic bands for high performance bulk thermoelectric," *Nature* 473, **66** (2011).

[ix] P. Jood, et al., "Al-doped zinc oxide nanocomposites with enhanced thermoelectric properties," *Nano Lett.*, **11** [9] (2011).

[x] J.G. Cheng, et al., "Spin fluctuations in the antiferromagnetic metal $Nb_{12}O_{29}$," *Phys. Rev. B.*, **80** (2009).

[xi] .E.L. Waldron, et al., "Structure and electronic properties of monoclinic $Nb_{12}O_{29}$," *J Phys. Chem. Solids,* **65** (2004).

[xii] R.J. Cava, et al., "Electrical and magnetic properties of $Nb_2O_{5-\delta}$ crystallographic shear structures," *Phys. Rev. B,* **44** (1991).

[xiii] J.F. Marucco, "Electrical resistance and defect structure of stable and metastable phases of the system $Nb_{12}O_{29}$–Nb_2O_5 between 800 and 1100 °C," *J. Chem. Phys*. **70** (1979).

[xiv] T. McQueen, Q. Xu, E.N. Andersen, H.W. Zandbergen, and R.J. Cava, "Structures of the reduced niobium oxides $Nb_{12}O_{29}$ and $Nb_{22}O_{54}$," *J. Solid State Chem.,* **180** (2007).

[xv] M. Llunell and P. Alemany, "Crystal Structure and Coexistanence of Localized and delocalized Electrons in $Nb_{12}O_{29}$," *J. Solid State Chem.,* **149** (2000)